

The giant anomalous Hall and Nernst effects in Kagome permanent magnets RCo_5

Weian Guo¹, Pengyu Zheng¹, Rui Liu¹, Yiran Peng¹, Ying Yang¹ and Zhiping Yin^{1,2*}

¹School of Physics & Astronomy and Center for Advanced Quantum Studies, Beijing Normal University, Beijing 100875, China

²Key Laboratory of Multiscale Spin Physics (Ministry of Education), Beijing Normal University, Beijing 100875, China

* Contact authors: yinzhiping@bnu.edu.cn

Abstract

Kagome lattice materials have attracted considerable attention due to their intriguing topological properties and potential applications in next-generation quantum and spintronic technologies. In particular, rare-earth permanent magnets with Kagome structure provide an ideal platform that combines robust magnetism with nontrivial quantum phenomena. However, their anomalous transport properties, particularly thermoelectric responses, remain insufficiently explored. In this work, we perform systematic first-principles calculations on the anomalous Hall and anomalous Nernst effects in Kagome permanent magnets RCo_5 ($R=Ce, La, Sm, Gd$). We find that $CeCo_5$ exhibits a pronounced anomalous Hall conductivity of $\sim 1500 \Omega^{-1}cm^{-1}$ while $GdCo_5$ displays a substantial anomalous Nernst conductivity of $11 A \cdot m^{-1} \cdot K^{-1}$ within ± 0.1 eV of the Fermi energy, both comparable to or surpassing the measured intrinsic values reported in many typical Weyl and Heusler magnets. These exceptional anomalous transport properties originate from Berry curvature hotspots near spin-orbital coupling induced band gaps. If validated, these theoretical predictions would be important for Berry-curvature-driven transport in magnetic intermetallic. Our results establish RCo_5 compounds as versatile platforms for exploring Berry curvature-driven transport in tunable magnetic topological materials.

I. Introduction

The rare-earth permanent magnets are generally referred to intermetallic compounds composed of rare-earth and transition-metal elements, such as $NdFeB$, $SmFeN$. These materials exhibit high coercivity and play a vital role in modern industries, including aerospace and microwave communications [1]. Kagome lattice materials, characterized by geometrically frustrated networks, have attracted considerable interest due to their abundant quantum phenomena, including spin liquid states [2–4] and fractional quantum Hall effect [5–7]. In addition, the Kagome lattice hosts flat bands and van Hove singularities (vHS) [6,8] which have been associated with unconventional superconductivity and charge density wave (CDW) [9–12]. When permanent magnets adopt a Kagome lattice structure, they simultaneously possess both high magnetic hardness and nontrivial topological properties [13–15]. Among the fertile Kagome materials, compounds such as RCo_5 ($R=rare\ earth$) crystallize in the $CaCu_5$ -type structure (space group $P6/mmm$), which can be regarded as an alternating stack of Kagome Co planes and rare-earth atomic layers stacked along c -axis. These compounds represent a typical class of permanent magnets with Kagome lattice.

The anomalous Hall effect (AHE), in contrast to the ordinary Hall effect, refers to a transverse current that arises in magnetic systems due to intrinsic magnetic moments and spin-orbit coupling (SOC) [16,17]. Analogously, when an electric field is replaced by a temperature gra-

dient, a transverse voltage drop can occur, known as the anomalous Nernst effect (ANE) [18]. Both AHE and ANE can originate from two distinct mechanisms: an intrinsic contribution, which is fundamentally related to Berry curvature (BC) of the electronic band structure and an extrinsic contribution, attributed to scattering processes such as skew scattering and side-jump mechanisms [19]. The intrinsic AHE, in particular, is directly linked to the anomalous velocity induced by the Berry phase, making the BC a central quantity in understanding topological transport phenomena [20,21].

Despite the growing understanding of Berry curvature-driven transport in various materials, most previous studies on Kagome lattice permanent magnets, namely RCO_5 family, have primarily focused on their magnetic properties [22–29]. Only a few investigations of AHE and ANE in this system were reported while many members of this family are still lack of study. For example, Ngo calculated AHE in $GdCo_5$ [30], while Asuka investigated the anomalous Ettingshausen and Nernst effects in $SmCo_5$ and $(Sm,Gd)Co_5$ alloys, initiating the concept of “thermoelectric permanent magnets” by linking magnetic materials to thermoelectric performance [31,32]. In contrast, magnetic topological semimetals—such as $GdPtBi$ [33], $Co_3Sn_2S_2$ [34], Mn_3Sn [35], and Co_2MnGa [18]—have been widely recognized as model systems for exploring large AHE and ANE responses. In these systems, both effects are understood to arise from pronounced Berry curvature near the Fermi level, often associated with SOC-induced gaps or symmetry-protected nodal lines. Notably, when mirror symmetry is broken in certain Heusler compounds, SOC can open a gap along nodal lines, leading to enhanced Berry curvature and strong intrinsic transport responses [36,37].

In this work, we present theoretical research on Kagome permanent magnets RCO_5 ($R=Ce, La, Sm, Gd$), focusing on their AHE and ANE. These four members are selected because they possess a fixed easy axis along the c -axis, unlike compounds with $R=Pr, Nd, Dy, Ho, and Tb$, which exhibit temperature-dependent spin reorientation transitions, with magnetization directions that vary across different temperature ranges. Our computational results reveal that all four members exhibit a large AHC within ± 0.1 eV of the Fermi energy, with $CeCo_5$ showing the highest value. Its peak AHC reaches 1500 S/cm at 0.084 eV below the Fermi energy. To identify the origin of the giant AHC, we carefully study the BC of each member in the first Brillouin zone and find that the main contributions of BC in $CeCo_5$ stem from the $k_z=0.2$ and $k_z=0.4$ planes. In these planes the BC is strongly concentrated on energy gaps opened by spin-orbital coupling which contributes significantly to the AHC. Analogously, $GdCo_5$ exhibits the highest ANC among the four compounds within ± 0.1 eV, reaching $11 \text{ A}\cdot\text{m}^{-1}\cdot\text{K}^{-1}$ at approximately 80 meV above the Fermi energy and the main contribution from BC also stems from the BC located at gaps opened by the SOC. Our work demonstrates the coexistence of pronounced anomalous Hall and anomalous Nernst effects within the same compound family—namely, Kagome permanent magnets—offering a valuable platform for studying anomalous transport phenomena.

II. Methods

A. Calculation of anomalous transport properties

The Berry curvature in the system is calculated by the Kubo formula [16,19,38]

$$\Omega_{ij}^n = i \sum_{m \neq n} \frac{\langle n | \frac{\partial H}{\partial k_i} | m \rangle \langle m | \frac{\partial H}{\partial k_j} | n \rangle - (i \leftrightarrow j)}{(E_n - E_m)^2} \quad (1)$$

where $|\psi\rangle$, E_n are eigenstate and eigenvalue of H , respectively. Given the Berry curvature, we can calculate the AHC via the Kubo formula [39]

$$\sigma_{ij} = \frac{e^2}{\hbar} \sum_n \int \frac{d^3k}{(2\pi)^3} \Omega_{ij}^n f_n \quad (2)$$

The ANC proposed by Xiao [40] can be obtained by

$$\alpha_{ij} = -\frac{1}{T} \frac{e}{\hbar} \sum_n \int \frac{d^3k}{(2\pi)^3} \Omega_{ij}^n \left[(E_n - E_F) f_n + k_B T \ln \left(1 + \exp \left(\frac{E_n - E_F}{-k_B T} \right) \right) \right] \quad (3)$$

here, T and f_n are the temperature and Fermi-Dirac distribution function, respectively. AHC and ANC can both be formulated within a unified theoretical framework as [37]:

$$\lambda_{ij} = \frac{e^2}{\hbar} \int \frac{d^3k}{(2\pi)^3} \Omega_{ij}^n w_\lambda(E_n - E_F), \quad \lambda = \sigma, \alpha \quad (4)$$

where w_σ and w_α are

$$w_\sigma(E) = f_n^T(E) \quad (5)$$

$$w_\alpha(E) = -\frac{1}{eT} \left[E f_n^T + k_B T \ln \left(1 + \exp \left(\frac{E}{-k_B T} \right) \right) \right] \quad (6)$$

here f_n^T is the Fermi-Dirac function at temperature T .

B. First-principles calculations

Electronic structure calculations were performed within the framework of density-functional theory (DFT), as implemented in Vienna Ab initio Simulation Package (VASP) [41]. The projector augmented wave (PAW) method was used to treat ionic potential, with the PAW_PBE datasets (POTCAR tags) Co (06Sep2000), Ce(04Sep2000), La(06Sep2000), Sm(17Dec2003), Gd(23Dec2003). The exchange-correlation potential was treated using the Perdew-Burke-Ernzerhof (PBE) form of the generalized gradient approximation (GGA) [42], with spin-orbital coupling included in all calculations in a fully noncollinear setup, and the spin quantization axis along [001].

The plane-wave cutoff of 500 eV was applied and Γ -centered Monkhorst-Pack mesh of $14 \times 14 \times 18$ was used for Brillouin-zone sampling. The convergence criterion for electronic self-consistency was set to 10^{-6} eV and Hellmann-Feynman forces were converged to less than 0.02 eV/Å. For the smearing scheme, the tetrahedron method with Blöchl corrections (ISMEAR = -5) was employed in all calculations to ensure accurate total energies and density of states.

Magnetic initial conditions were assigned according to the rare-earth and transition-metal sublattices, e.g., $\sim 5 \mu_B$ for Ce/La/Sm/Gd atoms and $\sim 2 \mu_B$ for Co atoms. Experimental crystal structures were adopted as reported in Refs. [24,28,43]. The values of the effective Hubbard U_{eff} (Hubbard U minus Hund's coupling J [44]) used in the calculations were 5.0 eV for Ce and La, and 6.0 eV for Sm and Gd, based on literature values [45–47] and were further tested to ensure reasonable agreement between the calculated and experimental magnetic moments [26].

The rare-earth $4f$ states were explicitly treated as valence electrons within the DFT+ U framework. Benchmark tests comparing the valence and open-core treatments are provided in the supplementary materials [48].

Based on the electronic structure, a tight-binding Hamiltonian was constructed using the maximally localized Wannier function (MLWF) method [49], as implemented in the Wannier90 package [50]. The d, f orbitals of R atoms and the s, p, d orbitals of Co atoms were selected as projectors for wannierization procedure.

Based on the wannierized tight-binding Hamiltonians, the AHC and ANC were calculated using the Kubo formula based on Eq. 2 and Eq. 3, as implemented in Wanniertools package [51] with a Lorentzian broadening parameter $\eta = 0.001$ eV at $T = 300$ K. The Berry curvature was integrated over Γ -centered meshes up to $101 \times 101 \times 101$.

To benchmark the reliability of our calculations, we extracted the spin and orbital contributions to the magnetic moments on the rare-earth and Co sites. The results, summarized in Table I, show that the calculated total magnetic moments per formula unit are in reasonable agreement with experimental values, validating the calculation setups.

Table I. Calculated magnetic moments of RCO_5 and experimental values. All quantities are in μ_B .

	Re moment (μ_B) (spin/orbital/total)	Co moment (μ_B) (spin/orbital/total)	Total moment (μ_B /f.u.)	Exp. (μ_B /f.u.)
CeCo ₅	-0.787/0.307/-0.480	7.109/0.662/7.771	7.291	~ 7.1 [52,53]
LaCo ₅	-0.206/0.023/-0.183	7.499/0.703/8.202	8.019	~ 8.1 [54,55]
SmCo ₅	5.132/-0.569/4.563	7.552/0.664/8.216	12.779	~ 12.15 [28] ~ 12.86 [56]
GdCo ₅	-7.296/-0.007/-7.303	7.814/0.607/8.421	1.118	~ 1.37 [57]

III. Results and discussion

A. Basic electronic structure of RCO_5

We first present the crystal structure and basic electronic structure of RCO_5 in Fig. 1. RCO_5 family crystallizes in a stacked $P6/mmm$ (No. 191) structure. R atoms occupy the center of hexagons in R -Co1 layers and Co2 layers form the Kagome lattice as shown in Fig. 1(a). The spin-summed band structure and density of states of CeCo₅, calculated with SOC are shown in the Fig. 1(c). The density of states reveals that the d -orbital component dominates near the Fermi level in CeCo₅, while the f -orbitals also contribute, primarily appearing above the Fermi level. (d)-(i) are the three-dimensional Fermi surface of the six individual bands crossing the Fermi level for CeCo₅. The other members' Fermi surfaces and band structures are shown in the supplementary materials [48].

In each branch of the Fermi surface of CeCo₅ as shown in (d)-(i), the weight of five d components is relatively uniform, while seven f components account for a large proportion in the fifth and sixth branches, contributing to the f states at the Fermi level in the DOS. From the band structure of the four members (see the supplementary materials [48]), we see that two sets of flat bands which are composed of Ce f orbitals located at around 0.6 eV above the Fermi level and Co d orbitals pinned at 0.4 eV below the Fermi level. The flat bands in RCO_5 differ significantly from those in AV_3Sb_5 compounds, where the flat bands, composed of d orbitals, are located above the Fermi level [58,59].

B. Anomalous Hall effect in RCo₅

Fig. 2(a)-(d) are calculated anomalous Hall conductivities of CeCo₅, LaCo₅, SmCo₅, GdCo₅, respectively. The CeCo₅, LaCo₅, SmCo₅ exhibit ferromagnetic ordering [24,28,61], whereas GdCo₅ adopts a ferrimagnetic configuration, in which Gd $4f$ moments are antiparallel to the Co $3d$ moments [23]. Here we utilize the experimental lattice parameters [24,28,43] and adopt different Hubbard U values from the literature [45–47] to fit the experimental magnetic moment [26]. From the calculated results, it is evident that all compounds exhibit giant values of AHC in the vicinity of the Fermi level, with CeCo₅ showing the largest magnitude reaching almost $1500 \Omega^{-1} \text{cm}^{-1}$.

In the calculations, all compounds were treated in collinear magnetic states with the spin quantization axis strictly along the crystallographic c axis. Specifically, LaCo₅, CeCo₅, and SmCo₅ were modeled as ferromagnets with all moments parallel to c , while GdCo₅ was modeled as a ferrimagnet and the net magnetization still aligned along c . Because the magnetization is strictly aligned c , the anomalous Hall and Nernst tensors reduce to an axial form with only

in-plane antisymmetric components being finite, while all out-of-plane components vanish by symmetry.

As illustrated in Fig. 3(a)-(d), CeCo₅—which exhibits the highest AHC—is selected as a representative compound for investigating the underlying mechanism. From previous research, we already know that AHC is directly related to Berry curvature and proportional to the sum of its integral over all occupied states below the Fermi level in the momentum space [16]. To better understand the underlying mechanism, we evaluate the BC distribution summed over all occupied states below the Fermi level on different k_z planes ranging from $k_z = 0$ to $k_z = 0.5$ in the first Brillouin zone (all k_z values are in the unit of $2\pi/c$). This allows us to clearly identify which part of the band structure contribute most significantly to the BC and further contribute to the AHC. We find that the BC is most pronounced on $k_z = 0.2$ and $k_z = 0.4$ planes, as shown in Fig. 3(a) and (c). The corresponding band structure on these planes are presented in Fig. 3(b) and (d), respectively.

As shown in Fig. 3(a), a ring-shaped region with strongly enhanced positive BC is observed around the Γ point in the first Brillouin zone (outlined by the blue solid line). This annular distribution resembles a gapped nodal line structure, but further confirmation is required, as will be discussed in the following section. In the corresponding band structure in Fig. 3(b), two band gaps can be observed along the Γ -M and Γ -K directions (highlighted by green circles), with the Fermi level lying within these gaps. Notably, the band located below the Fermi level contributes a positive BC, consistent with the ring-shaped distribution seen in Fig. 3(a).

On the $k_z = 0.4$ plane, the BC distribution exhibits a pattern similar to that on $k_z = 0.2$ plane. As shown in Fig. 3(c), a pronounced peak of BC appears along the Γ -K path close to the K point within the first Brillouin zone. In the corresponding band structure (Fig. 3(d)), a band gap is observed along the same Γ -K direction. The lower band at the gap position (i.e., below the Fermi level) contributes a positive BC (highlighted by the green circle), which corresponds to the BC hotspot near the Γ -K path in the BC distribution at $k_z = 0.4$.

To investigate the origin of the pronounced BC near the gap observed in Fig. 3, we analyzed the band structure on the corresponding k_z planes, as shown in Fig. 4(a)-(b). On the $k_z = 0.2$ plane, when SOC is taken into account, the crossing of spin-up and spin-down bands opens a band gap. This band crossing differs from that observed in Heusler compounds Fe₂MnX [36] and Co₃Sn₂S₂ [34], as it does not involve crossing within the same spin channel. Therefore, once the SOC opens the gap, no gapped nodal lines are formed as in Heusler compounds.

On the $k_z = 0.4$ plane, the band crossing is symmetry-protected in the absence of SOC. However, once SOC is introduced and a gap opens, the two bands forming the gap are no longer symmetry-protected, as confirmed by analyzing their irreducible representations. Actually, in regions where SOC induces band splitting, the Berry curvature becomes sharply localized near the resulting band gaps. This reflects one of the key intrinsic mechanisms underlying the giant AHE.

To provide an intuitive and quantitative understanding of the BC hotspots revealed in Fig. 3, we constructed two minimal models that simulate the SOC-induced band gap scenarios depicted in Fig. 5(a)-(b). These two cases correspond directly to the band structures analyzed in Fig. 4(a) and Fig. 4(b). Specifically, Fig. 5(a) reflects the ring-like Berry curvature distribution associated with the SOC-induced gap on the $k_z = 0.2$ plane shown in Fig. 3(a), whose underlying band structure is discussed in Fig. 4(a). Similarly, Fig. 5(b) captures the Dirac-type Berry curvature peak corresponding to the SOC-induced gap near the K point on the $k_z = 0.4$ plane, as analyzed in Fig. 3(c) and band structure of Fig. 4(b).

Fig. 5(a) shows the schematic band structure without spin-orbital coupling. In this case, the conduction and valence bands invert and form a nodal ring in the k_x - k_y plane. This nodal ring is protected by symmetry, and therefore, the Berry curvature remains strictly zero throughout the entire nodal ring. Upon introducing SOC, the degeneracy of the nodal ring is lifted, opening a gap along the ring. As a result, a ring-shaped distribution of sharply localized Berry curvature

emerges near the band gap. This pattern closely resembles the annular Berry curvature hotspot observed in the results shown in Fig. 3(a).

Fig. 5(b) illustrates a scenario where two linearly crossing bands form a Dirac-like dispersion at a single point in momentum space. Without SOC, the crossing remains gapless and the Berry curvature is absent. When SOC is introduced, a band gap opens at the crossing point and the Berry curvature becomes sharply peaked in the vicinity of this gap. This is consistent with the sharply localized Berry curvature peak observed along the Γ -K path in Fig. 3(c), which corresponds to the SOC-induced avoided crossing analyzed in Fig. 4(b).

The Berry curvature of a two-band model can be formally written as [16]:

$$\Omega^z(\mathbf{k}) = \frac{1}{2} \frac{\vec{h} \cdot (\partial_{k_x} \vec{h} \times \partial_{k_y} \vec{h})}{|\vec{h}|^3} \quad (7)$$

where $\vec{h}(\mathbf{k}) = (h_x, h_y, h_z)$ are the momentum-dependent coefficients of the Pauli matrices in the two-band Hamiltonian $H(\mathbf{k}) = h_x \sigma_x + h_y \sigma_y + h_z \sigma_z$. In our nodal ring model, $h_z(\mathbf{k}) = k^2 - k_0^2$ describes the band inversion that forms the ring, and SOC is introduced via a constant mass term $h_x = \Delta$. Assuming $h_y = 0$, the Berry curvature simplifies to

$$\Omega^z(k) = \frac{4\Delta r^2}{[(r^2 - k_0^2)^2 + \Delta^2]^{3/2}}, \quad (8)$$

where $r = \sqrt{k_x^2 + k_y^2}$. This analytic expression demonstrates that the Berry curvature is strongly peaked around the ring defined by $r = k_0$, forming a Berry curvature hot ring consistent with our numerical findings.

To complement this, we also examine a simpler 1D Dirac-type model. In the absence of SOC, the band structure consists of linear crossings at $k = 0$, and the Berry curvature vanishes. The energy dispersion in this case is given by

$$\varepsilon_{\pm} = \pm |k|, \quad (9)$$

which describes the massless Dirac fermions. When SOC is introduced, it opens a gap at the Dirac point. This is typically modeled by adding a mass term Δ , resulting in the massive Dirac Hamiltonian with energy eigenvalues

$$\varepsilon_{\pm}^{SOC} = \pm \sqrt{k^2 + \Delta^2}. \quad (10)$$

This dispersion reflects the lifting of degeneracy due to SOC.

The corresponding Berry curvature for the bands can be derived from the general two-band expression. For this model, the Berry curvature takes the form

$$\Omega^z(k) = \frac{\Delta}{(k^2 + \Delta^2)^{3/2}}. \quad (11)$$

This function is sharply localized around $k = 0$ and decays rapidly for larger k , characterizing the intrinsic anomalous Hall effect arising from SOC-induced band gaps.

Together, these two models establish a direct link between SOC-induced gap openings and the formation of sharply localized Berry curvature. These insights provide an intuitive and quantitative understanding of the intrinsic mechanism underlying the AHE in the RCO_5 family, particularly in $CeCo_5$, where the band topology and SOC jointly give rise to the observed giant anomalous transport response. For a more quantitative analysis of the Berry curvature dependence on SOC and band gap size, see supplementary Fig. S11 [48].

C. Anomalous Nernst effect in RCO_5

Fig. 6(a)-(d) show the ANC of RCO_5 compounds at 300 K. For $CeCo_5$ and $GdCo_5$, the ANC reaches maximum values of $-8 \text{ A} \cdot \text{m}^{-1} \cdot \text{K}^{-1}$ at approximately 30 meV below the Fermi level and $11 \text{ A} \cdot \text{m}^{-1} \cdot \text{K}^{-1}$ at around 80 meV above the Fermi level, respectively. At the Fermi level, the ANC are $-5.5 \text{ A} \cdot \text{m}^{-1} \cdot \text{K}^{-1}$ for $CeCo_5$ and $3.3 \text{ A} \cdot \text{m}^{-1} \cdot \text{K}^{-1}$ for $GdCo_5$. In contrast, the maxima for $LaCo_5$ and $SmCo_5$ are located at 0.11 eV and 0.12 eV above the Fermi level, as marked by the green dashed lines in Fig. 6(b) and Fig. 6(c).

Since experimental measurements of ANC are available for $LaCo_5$ and $SmCo_5$, we indicate not only the energy positions of their maximum peaks but also the ANC values exactly at the Fermi level to enable direct comparison with experiment. For $CeCo_5$ and $GdCo_5$ where experimental ANC data are not yet reported, we provide both the Fermi-level values and the nearby maxima, so that our predictions can serve as a reference for future measurements. Notably, the calculated ANC for $SmCo_5$ at the Fermi level is approximately $5.6 \text{ A} \cdot \text{m}^{-1} \cdot \text{K}^{-1}$, which is in reasonable agreement with the experimental value of $4.5 \text{ A} \cdot \text{m}^{-1} \cdot \text{K}^{-1}$ [32], supporting the validity of our computational results.

As shown in Eq. (3), the ANC also depends on the BC in momentum space. The explicit forms of Eq. (2)–(6) are provided in the *Methods* section and we summarize their physical meanings here for clarity. A comparison with the expression for the AHC in Eq. (2) reveals that the key difference between AHC and ANC lies in the weights multiplied by the BC. If both of them are expressed in a unified form, they can be written as in Eq. (4), where Eq. (5) and Eq. (6) define the corresponding weight functions for AHC and ANC, respectively.

From this unified formulation, it is evident that w_λ serves as the integral weight distribution function for the Berry curvature in both AHC and ANC, with the distinctions between the weight functions illustrated in Fig. S12. Specifically, w_σ ensures that the Berry curvature of all occupied states below the Fermi level contributes to the intrinsic AHC. In contrast, w_α reaches its maximum at the Fermi level and decays exponentially away from it, with the rate of decay being temperature-dependent. Consequently, only the Berry curvature within a narrow energy window near the Fermi level predominantly contributes to the ANC. Moreover, the expression for ANC explicitly involves temperature T , which influences the weight function w_α . At higher T , the weighting w_α gets broader, allowing electron states slightly above the Fermi level to contribute to the ANC as well.

Based on the results of AHC, we observe that large BC typically arises near gapped regions in the band structure. To clearly identify the band gaps that contribute significantly to the ANC, we multiply the BC by the weight function w_α in our calculation. By examining the band structure across different k_z planes, we identify particular band gaps that give rise to significant BC as illustrated in Fig. 7(a)-(h). This approach allows us to determine the key band structure features responsible for the ANC.

In Fig. 7, panels (a)-(h) show the energy and momentum-resolved Berry curvature distributions projected onto the band structures of the four compounds. The left column ((a), (c), (e), (g)) displays the BC with a narrow color scale (± 20) to clearly visualize the overall distribution across the entire band, while the right column ((b), (d), (f), (h)) uses a wider scale ($\pm 6 \times 10^3$) to highlight the band segments with the strongest BC contributions. The regions enclosed by black ellipses indicate the specific band gaps that give rise to significant BC near the Fermi level. Notably, these are also the global maxima of BC across all k_z planes from $k_z = 0$ to $k_z = 0.5$.

The BC values for $LaCo_5$ and $SmCo_5$ are taken at their original Fermi level, while for $CeCo_5$ and $GdCo_5$, the Fermi level is set to the energy positions of maximum ANC values marked in Fig. 6. For the four compounds, the net BC at these marked regions—obtained by summing the contributions from the two bands forming the gap—follows the order (in absolute value): $GdCo_5$ (-5531), $CeCo_5$ (4862), $SmCo_5$ (1595) and $LaCo_5$ (-1376).

According to Eq. (3), the ANC is directly proportional to the BC, which accounts for

the descending order of the calculated ANC values in Fig. 6: GdCo_5 (11.3), CeCo_5 (-8.1), SmCo_5 (-5.7) and LaCo_5 (5.0). Moreover, the overall sign difference between the BC and ANC—originating from the minus sign in Eq. (3)—is clearly manifested in our computational results, demonstrating the internal consistency of the theoretical framework.

D. Quantitative comparison of AHC and ANC in different compounds

Fig. 8 presents a comparative analysis of the AHC and ANC across different compounds. Here we emphasize that the comparison in Fig. 8 is restricted to intrinsic contributions governed by Berry curvature either from experiments or from theoretical calculations. As shown in Fig. 8(a), for most listed compounds, the theoretical and experimental values of intrinsic AHC exhibit reasonable agreement. This agreement indicates that the mechanism of intrinsic AHC governed by Berry curvature is consistent with experimental observations.

However, it should be noted that in some materials the experimentally measured AHC contains both extrinsic and intrinsic contributions, and the intrinsic components can differ substantially from the total value. For example, in KV_3Sb_5 [79], the extremely large AHC of ~ 15507 S/cm originated from extrinsic mechanisms, namely skew scattering, rather than from the intrinsic Berry curvature. In Ref. [80], the reported AHC of NdGaSi is about 1730 S/cm, while the intrinsic part amounts to ~ 1166 S/cm. Similarly, the experimentally measured AHC of $\text{Mn}_{3.2}\text{Ge}$ [81] is 1587 S/cm, whereas the calculated intrinsic value is only ~ 155.7 S/cm.

We also note that the exceptionally large ANC reported for MnBi [82] (~ 44 $\text{A}\cdot\text{m}^{-1}\cdot\text{K}^{-1}$ at 80 K) arises predominantly from extrinsic mechanisms such as magnon-drag, while at room temperature its ANC decreases to only $\sim 2\text{--}3$ $\text{A}\cdot\text{m}^{-1}\cdot\text{K}^{-1}$. In YbMnBi_2 [78], an ANC of about 10 $\text{A}\cdot\text{m}^{-1}\cdot\text{K}^{-1}$ is observed around 100 K. Therefore, when making such comparisons, it is essential to distinguish whether the experimental values correspond to intrinsic or extrinsic contributions.

Among the listed materials, CeCo_5 exhibits a pronounced theoretical AHC, on par with or exceeding that of the well-known Weyl semimetals such as $\text{Co}_3\text{Sn}_2\text{S}_2$ and Co_2MnGa . Considering the typical discrepancy between calculated and experimental values observed in these listed compounds, it is reasonable to expect that the experimental AHC of CeCo_5 should be slightly higher than, or at least comparable to those of $\text{Co}_3\text{Sn}_2\text{S}_2$ and Co_2MnGa .

Fig. 8(b) compares the ANC values among these materials. GdCo_5 displays a substantial ANC within the RCO_5 -type compounds, approaching or surpassing values observed in $\text{Co}_3\text{Sn}_2\text{S}_2$, Co_2MnGa , and numerous Heusler compounds reported in the literature.

Given that RCO_5 compounds are rare-earth permanent magnets with well-established fabrication processes, they offer excellent tunability via doping. For CeCo_5 , density-of-states analysis shows that hole doping would shift the Fermi level to the energy where AHC reaches its maximum. Similarly, for GdCo_5 , electron doping would shift the Fermi level to the energy at which the ANC reaches its maximum.

1 Conclusions

In summary, our first-principles predictions of the Kagome-structured rare-earth intermetallic compounds RCO_5 reveal that these materials exhibit exceptionally large Berry curvature-driven transport properties. In particular, CeCo_5 and GdCo_5 demonstrate notably large theoretical intrinsic AHC and ANC, respectively, comparable to or greater than those observed in many conventional ferromagnets and topological semimetals.

The theoretical intrinsic AHC of CeCo_5 is on par with or exceeds that of prototypical Weyl semimetals such as $\text{Co}_3\text{Sn}_2\text{S}_2$ and Co_2MnGa , while the ANC of GdCo_5 matches or exceeds values reported for numerous Heusler compounds in previous studies [83]. These predictions call for future experimental verifications.

These findings highlight RCO_5 compounds as a promising class of materials that simultaneously possess high structural stability, well-developed fabrication techniques, and substantial intrinsic transport coefficients. Moreover, the close agreement between theoretical and experimental AHC values across the RCO_5 family confirms that intrinsic Berry curvature mechanisms dominate in these systems.

Notably, the tunability of these transport properties via doping offers a practical route to optimize their performance for applications. The combination of high-coercivity permanent magnetism and topological transport phenomena in the RCO_5 -type family offers a fertile platform for designing advanced spintronic and thermoelectric devices. These results motivate targeted experiments to verify the predicted optima. Future experimental studies, particularly on doped RCO_5 , could further validate these findings and unlock their potential in next-generation devices.

Acknowledgements

This work was supported by the Fundamental Research Funds for the Central Universities (Grant No. 2243300003), the Innovation Program for Quantum Science and Technology (Grant No. 2021ZD0302800), and the National Natural Science Foundation of China (Grant No. 12074041). The calculations were carried out on the high-performance computing cluster of Beijing Normal University in Zhuhai.

Data Availability

The data that support the findings of this article are not publicly available upon publication because it is not technically feasible and/or the cost of preparing, depositing, and hosting the data would be prohibitive within the terms of this research project. The data are available from the authors upon reasonable request.

References

- [1] O. Gutfleisch, M. A. Willard, E. Brück, C. H. Chen, S. G. Sankar, and J. P. Liu, Magnetic Materials and Devices for the 21st Century: Stronger, Lighter, and More Energy Efficient, *Adv. Mater.* **23**, 821 (2011).
- [2] L. Balents, Spin liquids in frustrated magnets, *Nature* **464**, 199 (2010).
- [3] M. Fu, T. Imai, T.-H. Han, and Y. S. Lee, Evidence for a gapped spin-liquid ground state in a Kagome Heisenberg antiferromagnet, *Science* **350**, 655 (2015).
- [4] S. Yan, D. A. Huse, and S. R. White, Spin-Liquid Ground State of the $S = 1/2$ Kagome Heisenberg Antiferromagnet, *Science* **332**, 1173 (2011).
- [5] Z. Liu, F. Liu, and Y.-S. Wu, Exotic electronic states in the world of flat bands: From theory to material, *Chinese Phys. B* **23**, 077308 (2014).
- [6] E. Tang, J.-W. Mei, and X.-G. Wen, High-Temperature Fractional Quantum Hall States, *Phys. Rev. Lett.* **106**, 236802 (2011).
- [7] T. Neupert, L. Santos, C. Chamon, and C. Mudry, Fractional Quantum Hall States at Zero Magnetic Field, *Phys. Rev. Lett.* **106**, 236804 (2011).
- [8] Z. Lin, J. H. Choi, Q. Zhang, W. Qin, S. Yi, P. Wang, L. Li, Y. Wang, H. Zhang, Z. Sun *et al.*, Flatbands and Emergent Ferromagnetic Ordering in Fe_3Sn_2 Kagome Lattices, *Phys. Rev. Lett.* **121**, 096401 (2018).

- [9] W.-H. Ko, P. A. Lee, and X.-G. Wen, Doped kagome system as exotic superconductor, *Phys. Rev. B* **79**, 214502 (2009).
- [10] S.-L. Yu and J.-X. Li, Chiral superconducting phase and chiral spin-density-wave phase in a Hubbard model on the kagome lattice, *Phys. Rev. B* **85**, 144402 (2012).
- [11] M. L. Kiesel, C. Platt, and R. Thomale, Unconventional Fermi Surface Instabilities in the Kagome Hubbard Model, *Phys. Rev. Lett.* **110**, 126405 (2013).
- [12] W.-S. Wang, Z.-Z. Li, Y.-Y. Xiang, and Q.-H. Wang, Competing electronic orders on kagome lattices at van Hove filling, *Phys. Rev. B* **87**, 115135 (2013).
- [13] N. Chowdhury, K. I. A. Khan, H. Bangar, P. Gupta, R. S. Yadav, R. Agarwal, A. Kumar, and P. K. Muduli, Kagome Magnets: The Emerging Materials for Spintronic Memories, *Proc. Natl. Acad. Sci., India, Sect. A Phys. Sci.* **93**, 477 (2023).
- [14] H. R. Kirchmayr, Permanent magnets and hard magnetic materials, *J. Phys. D: Appl. Phys.* **29**, 2763 (1996).
- [15] J.-X. Yin, B. Lian, and M. Z. Hasan, Topological kagome magnets and superconductors, *Nature* **612**, 647 (2022).
- [16] D. Xiao, M.-C. Chang, and Q. Niu, Berry phase effects on electronic properties, *Rev. Mod. Phys.* **82**, 1959 (2010).
- [17] S. Onoda, N. Sugimoto, and N. Nagaosa, Intrinsic Versus Extrinsic Anomalous Hall Effect in Ferromagnets, *Phys. Rev. Lett.* **97**, 126602 (2006).
- [18] A. Sakai, Y. P. Mizuta, A. A. Nugroho, R. Sihombing, T. Koretsune, M.-T. Suzuki, N. Takemori, R. Ishii, D. N.-Hamane, R. Arita *et al.*, Giant anomalous Nernst effect and quantum-critical scaling in a ferromagnetic semimetal, *Nat. Phys.* **14**, 1119 (2018).
- [19] N. Nagaosa, J. Sinova, S. Onoda, A. H. MacDonald, and N. P. Ong, Anomalous Hall effect, *Rev. Mod. Phys.* **82**, 1539 (2010).
- [20] G. Sundaram and Q. Niu, Wave-packet dynamics in slowly perturbed crystals: Gradient corrections and Berry-phase effects, *Phys. Rev. B* **59**, 14915 (1999).
- [21] M.-C. Chang and Q. Niu, Berry Phase, Hyperorbits, and the Hofstadter Spectrum, *Phys. Rev. Lett.* **75**, 1348 (1995).
- [22] C. E. Patrick, S. Kumar, G. Balakrishnan, R. S. Edwards, M. R. Lees, E. M.-Tapia, L. Petit, and J. B. Staunton, Rare-earth/transition-metal magnetic interactions in pristine and (Ni, Fe)-doped YCo₅ and GdCo₅, *Phys. Rev. Materials* **1**, 024411 (2017).
- [23] C. E. Patrick, S. Kumar, G. Balakrishnan, R. S. Edwards, M. R. Lees, L. Petit, and J. B. Staunton, Calculating the Magnetic Anisotropy of Rare-Earth–Transition-Metal Ferrimagnets, *Phys. Rev. Lett.* **120**, 097202 (2018).
- [24] L. Nordström, O. Eriksson, M. S. S. Brooks, and B. Johansson, Theory of ferromagnetism in CeCo₅, *Phys. Rev. B* **41**, 9111 (1990).
- [25] S. A. Nikitin, K. P. Skokov, Y. S. Koshkid'ko, Y. G. Pastushenkov, and T. I. Ivanova, Giant Rotating Magnetocaloric Effect in the Region of Spin-Reorientation Transition in the NdCo₅ Single Crystal, *Phys. Rev. Lett.* **105**, 137205 (2010).

- [26] C. E. Patrick and J. B. Staunton, Rare-earth/transition-metal magnets at finite temperature: Self-interaction-corrected relativistic density functional theory in the disordered local moment picture, *Phys. Rev. B* **97**, 224415 (2018).
- [27] Z. T.-Song, J. H.-Min, G. G.-Hua, H. X.-Feng, and C. Hong, Magnetic properties of R ions in $R\text{Co}_5$ compounds ($R = \text{Pr}, \text{Nd}, \text{Sm}, \text{Gd}, \text{Tb}, \text{Dy}, \text{Ho}, \text{and Er}$), *Phys. Rev. B* **43**, 8593 (1991).
- [28] H. Kohlmann, T. C. Hansen, and V. Nassif, Magnetic Structure of SmCo_5 from 5 K to the Curie Temperature, *Inorg. Chem.* **57**, 1702 (2018).
- [29] C. Fang, Z. Yan, X. Zhang, J. Xiao, F. Wang, and X. Xu, Effect of element doping on the structural stability, magnetic properties and electronic structure of SmCo_5 -based rare earth permanent magnets, *J. Magn. Magn. Mater.* **609**, 172492 (2024).
- [30] N. T. Hai, J.-C. Wu, J.-P. Chou, and J. Pothan, Novel anomalous Hall effect mechanism in ferrimagnetic GdCo alloy, *J. Appl. Phys.* **133**, 233901 (2023).
- [31] A. Miura, K. Masuda, T. Hirai, R. Iguchi, T. Seki, Y. Miura, H. Tsuchiura, K. Takanashi, and K. Uchida, High-temperature dependence of anomalous Ettingshausen effect in SmCo_5 -type permanent magnets, *Appl. Phys. Lett.* **117**, 082408 (2020).
- [32] A. Miura, H. S.-Amin, K. Masuda, H. Tsuchiura, Y. Miura, R. Iguchi, Y. Sakuraba, J. Shiomi, K. Hono, and K. Uchida, Observation of anomalous Ettingshausen effect and large transverse thermoelectric conductivity in permanent magnets, *Appl. Phys. Lett.* **115**, 222403 (2019).
- [33] C. Shekhar, N. Kumar, V. Grinenko, S. Singh, R. Sarkar, H. Luetkens, S.-C. Wu, Y. Zhang, A. C. Komarek, E. Kampert *et al.*, Anomalous Hall effect in Weyl semimetal half-Heusler compounds RPtBi ($R = \text{Gd}$ and Nd), *Proc. Natl. Acad. Sci. U.S.A.* **115**, 9140 (2018).
- [34] E. Liu, Y. Sun, N. Kumar, L. Muechler, A. Sun, L. Jiao, S.-Y. Yang, D. Liu, A. Liang, Q. Xu *et al.*, Giant anomalous Hall effect in a ferromagnetic kagome-lattice semimetal, *Nat. Phys.* **14**, 1125 (2018).
- [35] M. Ikhlas, T. Tomita, T. Koretsune, M.-T. Suzuki, D. N.-Hamane, R. Arita, Y. Otani, and S. Nakatsuji, Large anomalous Nernst effect at room temperature in a chiral antiferromagnet, *Nat. Phys.* **13**, 1085 (2017).
- [36] J. Noky, Q. Xu, C. Felser, and Y. Sun, Large anomalous Hall and Nernst effects from nodal line symmetry breaking in Fe_2MnX ($X = \text{P}, \text{As}, \text{Sb}$), *Phys. Rev. B* **99**, 165117 (2019).
- [37] J. Noky, J. Gooth, C. Felser, and Y. Sun, Characterization of topological band structures away from the Fermi level by the anomalous Nernst effect, *Phys. Rev. B* **98**, 241106 (2018).
- [38] D. J. Thouless, M. Kohmoto, M. P. Nightingale, and M. Den Nijs, Quantized Hall Conductance in a Two-Dimensional Periodic Potential, *Phys. Rev. Lett.* **49**, 405 (1982).
- [39] P. Wang, Z. Hu, X. Wu, and Q. Liu, Rational design of large anomalous Nernst effect in Dirac semimetals, *NPJ Comput. Mater.* **9**, 203 (2023).
- [40] D. Xiao, Y. Yao, Z. Fang, and Q. Niu, Berry-Phase Effect in Anomalous Thermoelectric Transport, *Phys. Rev. Lett.* **97**, 026603 (2006).
- [41] G. Kresse and J. Furthmüller, Efficient iterative schemes for *ab initio* total-energy calculations using a plane-wave basis set, *Phys. Rev. B* **54**, 11169 (1996).

- [42] J. P. Perdew, K. Burke, and M. Ernzerhof, Generalized Gradient Approximation Made Simple, *Phys. Rev. Lett.* **77**, 3865 (1996).
- [43] W. A. J. J. Velge and K. H. J. Buschow, Magnetic and Crystallographic Properties of Some Rare Earth Cobalt Compounds with CaZn_5 Structure, *J. Appl. Phys.* **39**, 1717 (1968).
- [44] S. L. Dudarev, G. A. Botton, S. Y. Savrasov, C. J. Humphreys, and A. P. Sutton, Electron-energy-loss spectra and the structural stability of nickel oxide: An LSDA+ U study, *Phys. Rev. B* **57**, 1505 (1998).
- [45] R. Xie and H. Zhang, Mixed valence nature of the Ce4f state in CeCo_5 based on spin-polarized DFT + DMFT calculations, *Phys. Rev. B* **106**, 224411 (2022).
- [46] B. Das, R. Choudhary, R. Skomski, B. Balasubramanian, A. K. Pathak, D. Paudyal, and D. J. Sellmyer, Anisotropy and orbital moment in Sm–Co permanent magnets, *Phys. Rev. B* **100**, 024419 (2019).
- [47] M. Mahdi, A. Djabri, M. M. Koc, R. Boukhalfa, M. Erkovan, Y. Chumakov, and F. Chemam, *Ab initio* study of GdCo_5 magnetic and magneto-optical properties, *Mater. Sci.-Poland* **37**, 182 (2019).
- [48] See supplementary materials for details of the electronic structures of the RCo_5 family and the robustness test of AHC/ANC with respect to Hubbard U and Berry curvature analysis of RCo_5 as well as the mechanism of Berry curvature in RCo_5 . The summary of the AHC/ANC for other materials was also included.
- [49] N. Marzari, A. A. Mostofi, J. R. Yates, I. Souza, and D. Vanderbilt, Maximally localized Wannier functions: Theory and applications, *Rev. Mod. Phys.* **84**, 1419 (2012).
- [50] A. A. Mostofi, J. R. Yates, Y.-S. Lee, I. Souza, D. Vanderbilt, and N. Marzari, wannier90: A tool for obtaining maximally-localised Wannier functions, *Comput. Phys. Commun.* **178**, 685 (2008).
- [51] Q. Wu, S. Zhang, H.-F. Song, M. Troyer, and A. A. Soluyanov, WannierTools: An open-source software package for novel topological materials, *Comput. Phys. Commun.* **224**, 405 (2018).
- [52] M. I. Bartashevich, T. Goto, R. J. Radwanski, and A. V. Korolyov, Magnetic anisotropy and high-field magnetization process of CeCo_5 , *J. Magn. Magn. Mater.* **131**, 61 (1994).
- [53] L. Ke, D. A. Kukusta, and D. D. Johnson, Origin of magnetic anisotropy in doped $\text{Ce}_2\text{Co}_{17}$ alloys, *Phys. Rev. B* **94**, 144429 (2016).
- [54] S. Xu, L. Zhou, S.-X. Li, X.-Y. Zeng, C. Jiang, J.-J. Mi, Z. Li, T.-L. Xia, and Z.-A. Xu, Anomalous Nernst effect in honeycomb and kagome magnet LaCo_5 at room temperature, *Mater. Today Phys.* **38**, 101269 (2023).
- [55] O. Moze, L. Pareti, A. Paoluzi, and K. H. J. Buschow, Magnetic structure and anisotropy of Ga- and Al-substituted LaCo_5 and YCo_5 intermetallics, *Phys. Rev. B* **53**, 11550 (1996).
- [56] S. K. Haider, H. M. Ngo, D. Kim, and Y. S. Kang, Enhancement of anisotropy energy of SmCo_5 by ceasing the coupling at 2c sites in the crystal lattice with Cu substitution, *Sci. Rep.* **11**, 10063 (2021).
- [57] A. L. Tedstone, C. E. Patrick, S. Kumar, R. S. Edwards, M. R. Lees, G. Balakrishnan, and J. B. Staunton, Structural and magnetic properties of $\text{GdCo}_{5-x}\text{Ni}_x$, *Phys. Rev. Materials* **3**, 034409 (2019).

- [58] M. Kang, S. Fang, J.-K. Kim, B. R. Ortiz, S. H. Ryu, J. Kim, J. Yoo, G. Sangiovanni, D. D. Sante, B.-G. Park *et al.*, Twofold van Hove singularity and origin of charge order in topological kagome superconductor CsV₃Sb₅, *Nat. Phys.* **18**, 301 (2022).
- [59] M. Liu, Z. Wang, and J.-J. Zhou, Weak electronic correlations in the kagome superconductor AV₃Sb₅ (A = K, Rb, Cs), *Phys. Rev. B* **105**, 235130 (2022).
- [60] K. Momma and F. Izumi, VESTA 3 for three-dimensional visualization of crystal, volumetric and morphology data, *J. Appl. Crystallogr.* **44**, 1272 (2011).
- [61] M. Brouha and K. H. J. Buschow, Magnetic properties and pressure dependence of the Curie temperature of LaCo_{5-x}Cu_{5-x}, *J. Appl. Phys.* **46**, 1355 (1975).
- [62] X. Li, L. Xu, L. Ding, J. Wang, M. Shen, X. Lu, Z. Zhu, and K. Behnia, Anomalous Nernst and Righi-Leduc effects in Mn₃Sn: Berry curvature and entropy flow, *Phys. Rev. Lett.* **119**, 056601 (2017).
- [63] L. Ye, M. Kang, J. Liu, F. von Cube, C. R. Wicker, T. Suzuki, C. Jozwiak, A. Bostwick, E. Rotenberg, D. C. Bell *et al.*, Massive Dirac fermions in a ferromagnetic kagome metal, *Nature* **555**, 638 (2018).
- [64] D. Zhu, J. Lu, Y. Jiang, Z. Zheng, D. Wang, C. Zhou, J. Zhou, S. Chen, Y. Gu, L. Liu *et al.*, Observation of anomalous Hall effect in collinear antiferromagnet IrMn, *Nano Lett.* **25**, 4307 (2025).
- [65] B. K. Hazra, M. M. Raja, R. Rawat, A. Lakhani, S. N. Kaul, and S. Srinath, Effect of disorder on the anomalous Hall conductivity of Co₂FeSi thin films, *J. Magn. Magn. Mater.* **448**, 371 (2018).
- [66] H.-L. Huang, J.-C. Tung, and G.-Y. Guo, Anomalous Hall effect and current spin polarization in Co₂FeX Heusler compounds (X = Al, G, In, Si, Ge, and Sn): A systematic *ab initio* study, *Phys. Rev. B* **91**, 134409 (2015).
- [67] A. K. Nayak, J. E. Fischer, Y. Sun, B. Yan, J. Karel, A. C. Komarek, C. Shekhar, N. Kumar, W. Schnelle, J. Kübler *et al.*, Large anomalous Hall effect driven by a nonvanishing Berry curvature in the noncollinear antiferromagnet Mn₃Ge, *Sci. Adv.* **2**, e1501870 (2016).
- [68] M. Liu, L. Ma, G. Li, C. Zhen, D. Hou, and D. Zhao, Extrinsic suppression of the anomalous Hall effect in the Fe-rich kagome magnet Fe₃Sn, *Phys. Rev. B* **111**, 094429 (2025).
- [69] X. Fu, J. Yu, Q. Zhang, Z. Li, and Z. Liu, The magnetic property and anomalous Hall effect of polycrystalline Fe₃Sn, *J. Phys. Chem. Solids* **198**, 112473 (2025).
- [70] C. Zeng, Y. Yao, Q. Niu, and H. H. Weitering, Linear Magnetization Dependence of the Intrinsic Anomalous Hall Effect, *Phys. Rev. Lett.* **96**, 037204 (2006).
- [71] Y. Yao, L. Kleinman, A. H. MacDonald, J. Sinova, T. Jungwirth, D. Wang, E. Wang, and Q. Niu, First Principles Calculation of Anomalous Hall Conductivity in Ferromagnetic bcc Fe, *Phys. Rev. Lett.* **92**, 037204 (2004).
- [72] S. N. Guin, K. Manna, J. Noky, S. J. Watzman, C. Fu, N. Kumar, W. Schnelle, C. Shekhar, Y. Sun, J. Gooth *et al.*, Anomalous Nernst effect beyond the magnetization scaling relation in the ferromagnetic Heusler compound Co₂MnGa, *NPJ Asia Mater.* **11**, 16 (2019).
- [73] Y. Hirokane, Y. Tomioka, Y. Imai, A. Maeda, and Y. Onose, Longitudinal and transverse thermoelectric transport in MnSi, *Phys. Rev. B* **93**, 014436 (2016).

- [74] T. Miyasato, N. Abe, T. Fujii, A. Asamitsu, S. Onoda, Y. Onose, N. Nagaosa, and Y. Tokura, Crossover behavior of the anomalous Hall effect and anomalous Nernst effect in itinerant ferromagnets, *Phys. Rev. Lett.* **99**, 086602 (2007).
- [75] T. Asaba, V. Ivanov, S. M. Thomas, S. Y. Savrasov, J. D. Thompson, E. D. Bauer, and F. Ronning, Colossal anomalous Nernst effect in a correlated noncentrosymmetric kagome ferromagnet, *Sci. Adv.* **7**, eabf1467 (2021).
- [76] H. Yang, W. You, J. Wang, J. Huang, C. Xi, X. Xu, C. Cao, M. Tian, Z.-A. Xu, J. Dai *et al.*, Giant anomalous Nernst effect in the magnetic Weyl semimetal $\text{Co}_3\text{Sn}_2\text{S}_2$, *Phys. Rev. Materials* **4**, 024202 (2020).
- [77] M. Li, H. Pi, Y. Zhao, T. Lin, Q. Zhang, X. Hu, C. Xiong, Z. Qiu, L. Wang, Y. Zhang *et al.*, Large anomalous Nernst effects at room temperature in Fe_3Pt thin films, *Adv. Mater.* **35**, 2301339 (2023).
- [78] Y. Pan, C. Le, B. He, S. J. Watzman, M. Yao, J. Gooth, J. P. Heremans, Y. Sun, and C. Felser, Giant anomalous Nernst signal in the antiferromagnet YbMnBi_2 , *Nat. Mater.* **21**, 203 (2022).
- [79] S.-Y. Yang, Y. Wang, B. R. Ortiz, D. Liu, J. Gayles, E. Derunova, R. G. Hernandez, L. Smejkal, Y. Chen, S. S. P. Parkin *et al.*, Giant unconventional anomalous Hall effect in the metallic frustrated magnet candidate KV_3Sb_5 , *Sci. Adv.* **6**, eabb6003 (2020).
- [80] A. Saraswati, S. Chatterjee, and N. Kumar, Giant anisotropic anomalous Hall effect in antiferromagnetic topological metal NdGaSi , arXiv:2409.06250.
- [81] J. S. R. McCoombs, B. D. MacNeil, V. Askarpour, J. Myra, H. Herdin, M. Pula, M. D. Robertson, G. M. Luke, K. L. Kavanagh, J. Maassen *et al.*, Giant anomalous Hall effect in epitaxial Mn_3Ge films with a cubic kagome structure, *Phys. Rev. B* **110**, 064401 (2024).
- [82] B. He, C. Şahin, S. R. Boona, B. C. Sales, Y. Pan, C. Felser, M. E. Flatté, and J. P. Heremans, Large magnon-induced anomalous Nernst conductivity in single-crystal MnBi , *Joule* **5**, 3057 (2021).
- [83] J. Noky, Y. Zhang, J. Gooth, C. Felser, and Y. Sun, Giant anomalous Hall and Nernst effect in magnetic cubic Heusler compounds, *NPJ Comput. Mater.* **6**, 77 (2020).

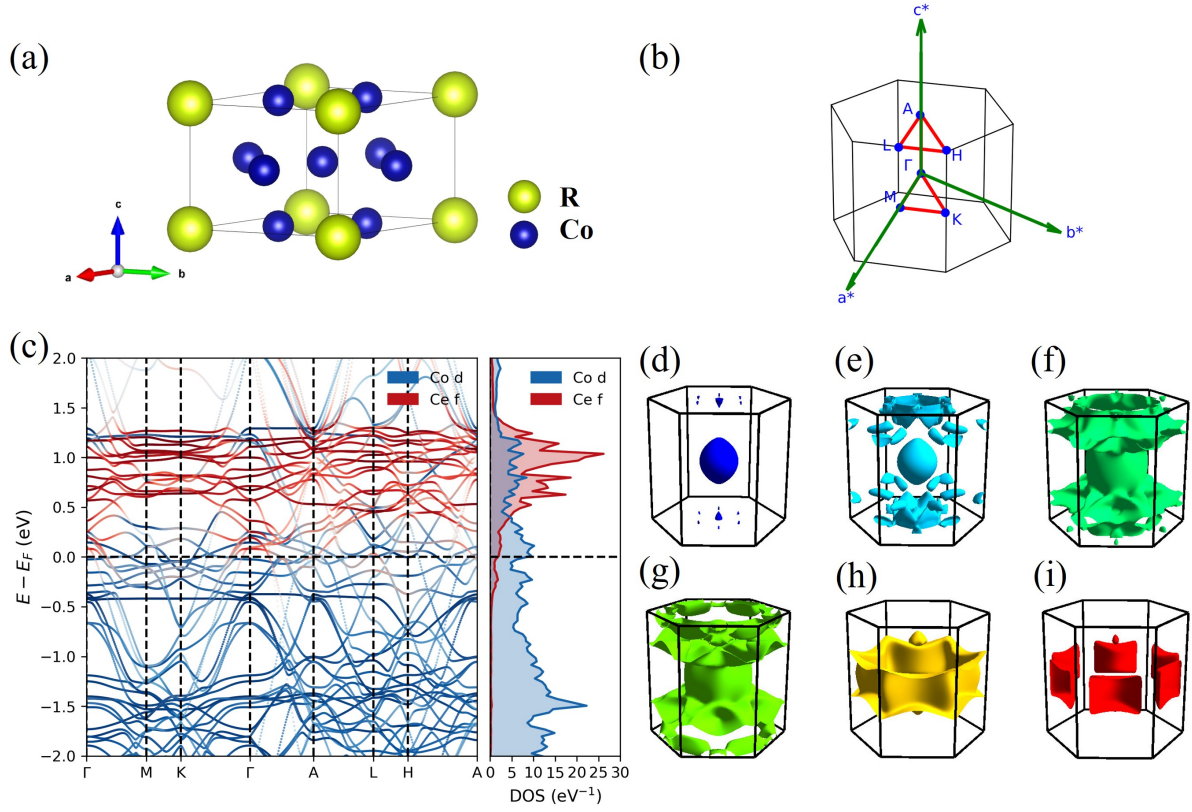


Figure 1: Crystal and electronic structure of RCo_5 . (a) Crystal structure of RCo_5 compounds constructed with the VESTA program [60]. (b) The first Brillouin zone and high-symmetry lines. (c) Spin-summed band structure and density of states of $CeCo_5$, calculated with spin-orbit coupling (SOC). (d)-(i) present the three-dimensional Fermi surfaces of the six bands crossing the Fermi level in $CeCo_5$.

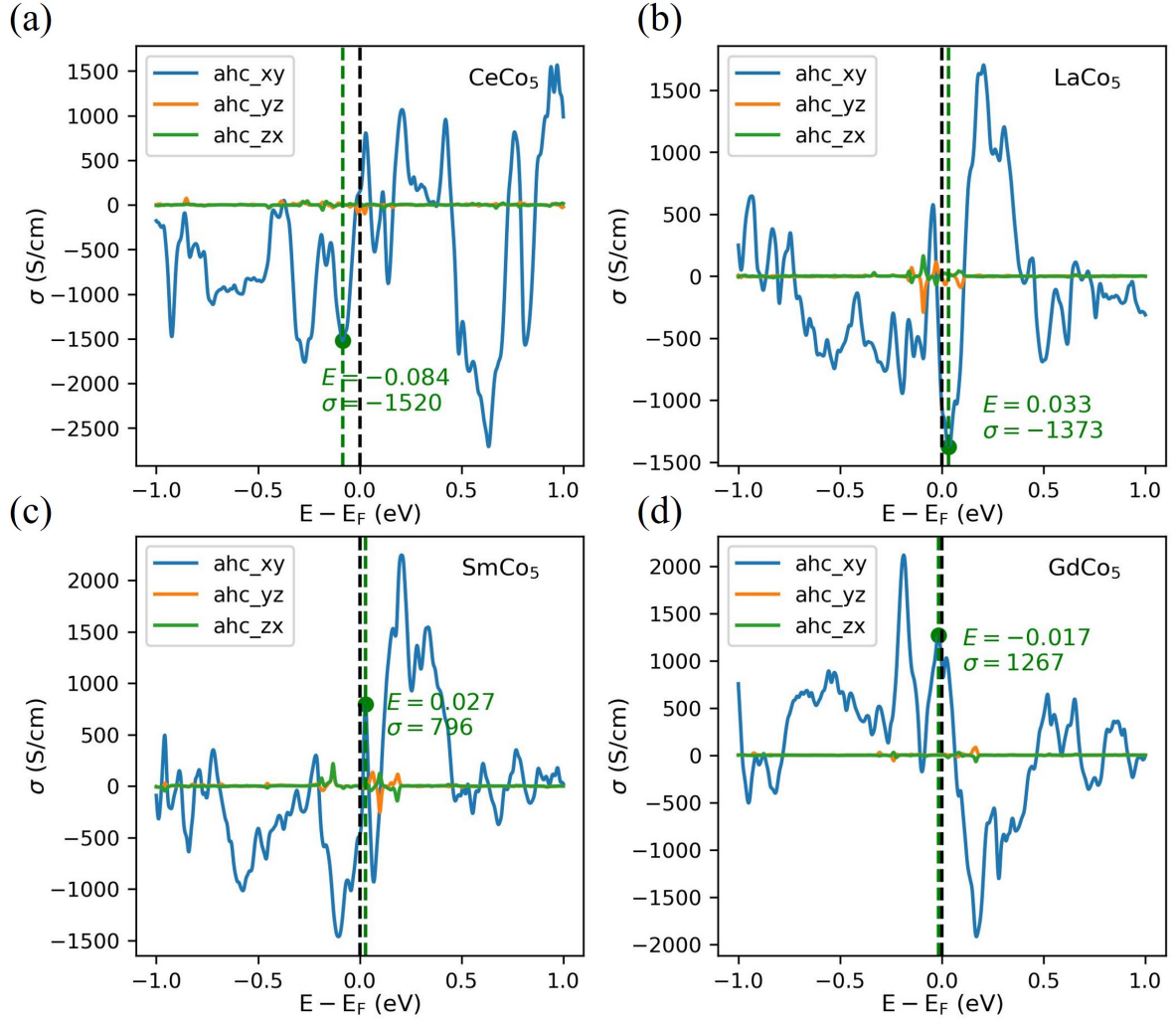


Figure 2: Calculated anomalous Hall conductivity (AHC) for CeCo₅ (a), LaCo₅ (b), SmCo₅ (c), and GdCo₅ (d), respectively. The green lines highlight the maximum AHC values within ± 0.1 eV of the Fermi level for each compound, with the corresponding energy positions and magnitudes indicated by green circles.

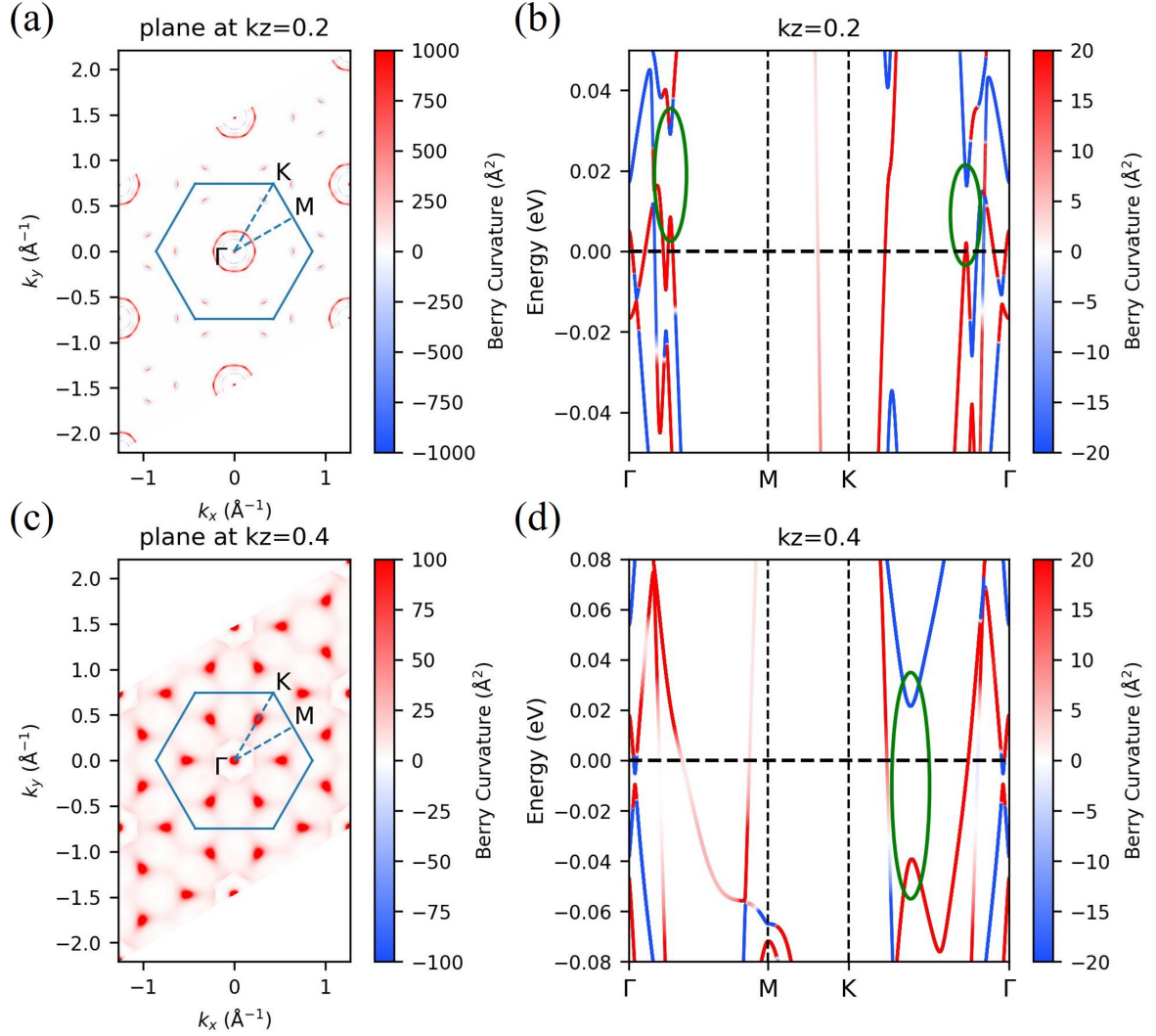


Figure 3: Berry curvature analyses of CeCo₅. (a, c) The Berry curvature distributions on the $k_z = 0.2$ and $k_z = 0.4$ planes of the Brillouin zone, respectively. Panels (b, d) are the corresponding band structures along the Γ -M-K- Γ path colored by the values of the Berry curvature. The positions marked by green ellipses correspond to the Berry curvature hotspots in panels (a) and (c).

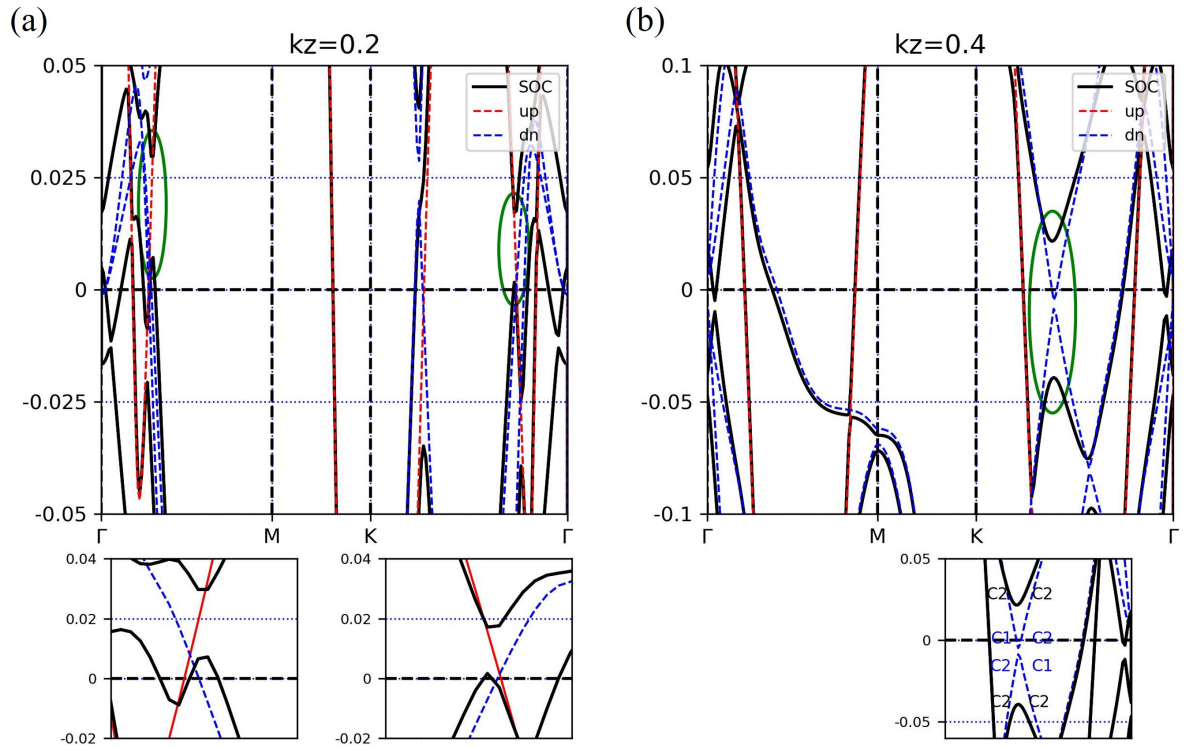


Figure 4: Band structure and symmetry analysis. (a) and (b) are the band structures with $k_z = 0.2$ and $k_z = 0.4$, respectively. The lower row shows zoomed-in views of the regions enclosed by green ellipses in the upper panel. The lower panel of (b) also shows the irreducible representations of the bands.

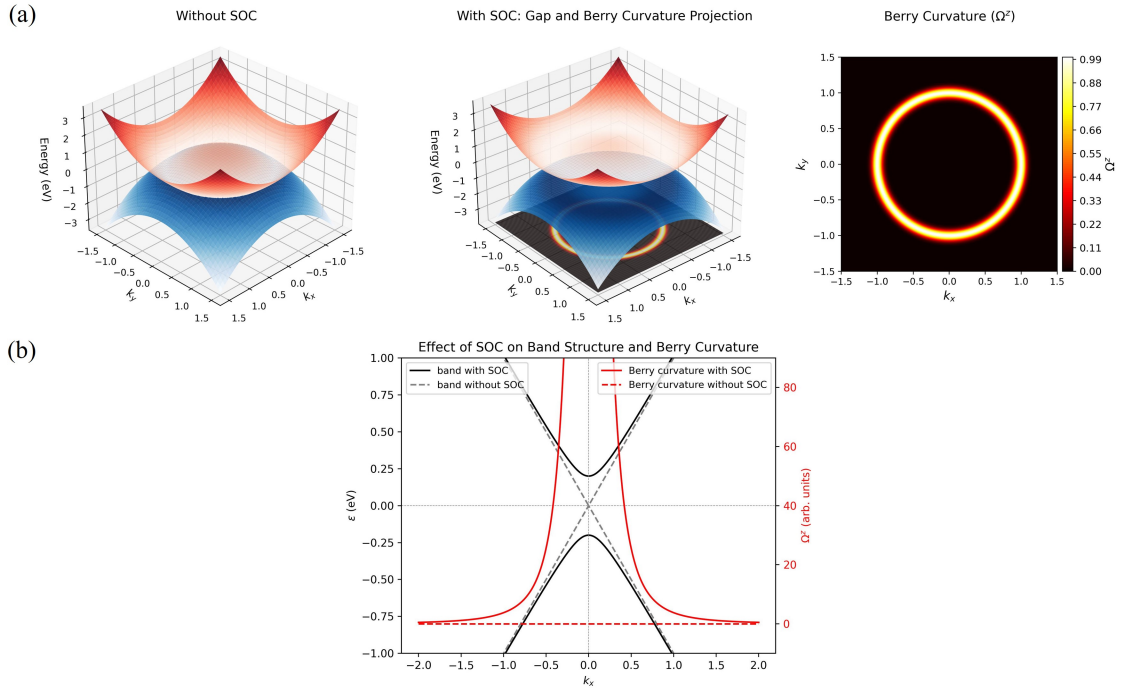


Figure 5: Schematic models illustrating the origin of the Berry curvature from SOC-induced band gaps. (a) Band inversion forms a nodal ring without SOC (left panel), with vanishing Berry curvature across the momentum space (middle panel). Right panel: SOC opens a gap along the ring, generating a ring-like Berry curvature hotspot. (b) Two linear bands cross at a Dirac point. SOC lifts the degeneracy and induces a peaked Berry curvature centered at the gap. These two mechanisms correspond to the scenarios in Fig. 4(a)–(b) and account for the Berry curvature distributions shown in Fig. 3(a) and Fig. 3(c), respectively.

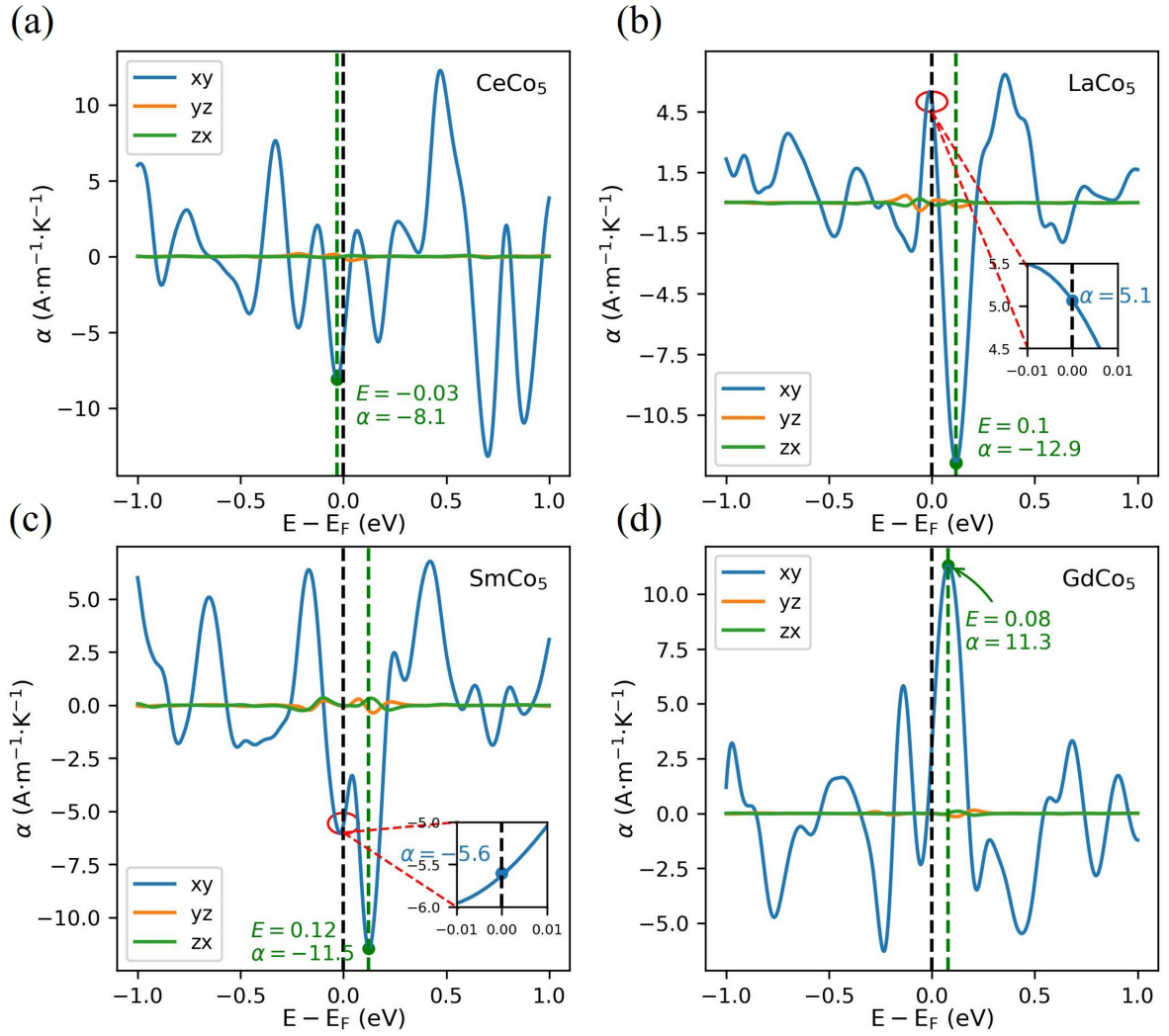


Figure 6: Calculated anomalous Nernst conductivity (ANC) for CeCo₅ (a), LaCo₅ (b), SmCo₅ (c), and GdCo₅ (d). The green lines and dots indicate the maximum values within ± 0.1 eV of the Fermi level. The insets of (b) and (c) show ANC values at the Fermi level.

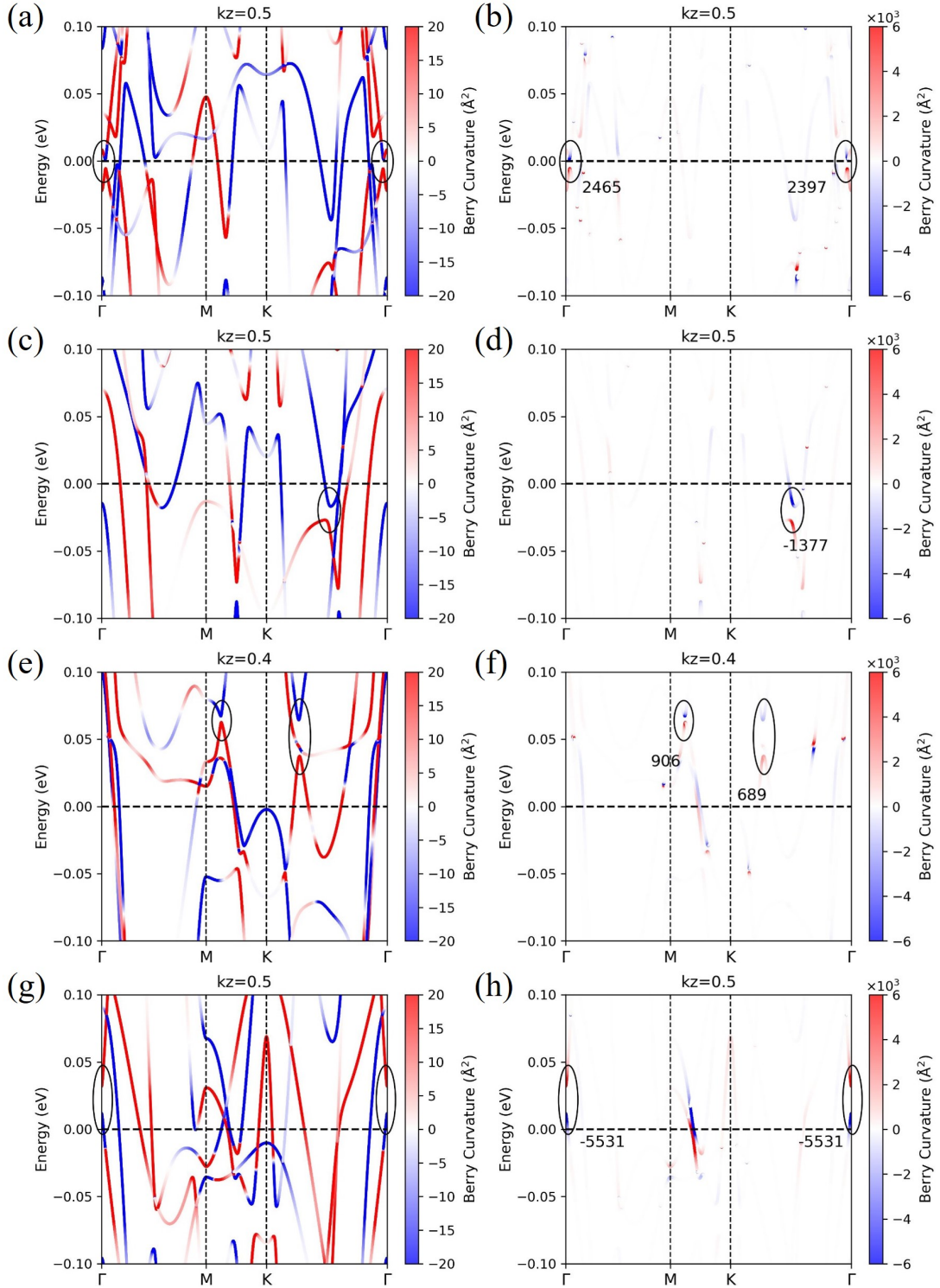


Figure 7: Band-resolved Berry curvature analysis of RCo_5 for ANC. Panels (a)–(b): $CeCo_5$ ($k_z = 0.5$); (c)–(d): $LaCo_5$ ($k_z = 0.5$); (e)–(f): $SmCo_5$ ($k_z = 0.4$); and (g)–(h): $GdCo_5$ ($k_z = 0.5$). Panels (a), (c), (e), and (g) display the band structures along the Γ –M–K– Γ path, colored by the values of the Berry curvature with a narrow color scale to provide a clearer view of the overall distribution, while the right panels (b), (d), (f), and (h) use a broader color scale to emphasize regions with the largest values. Black ellipses indicate locations where the Berry curvature reaches global maxima within the range $k_z = 0$ to $k_z = 0.5$.

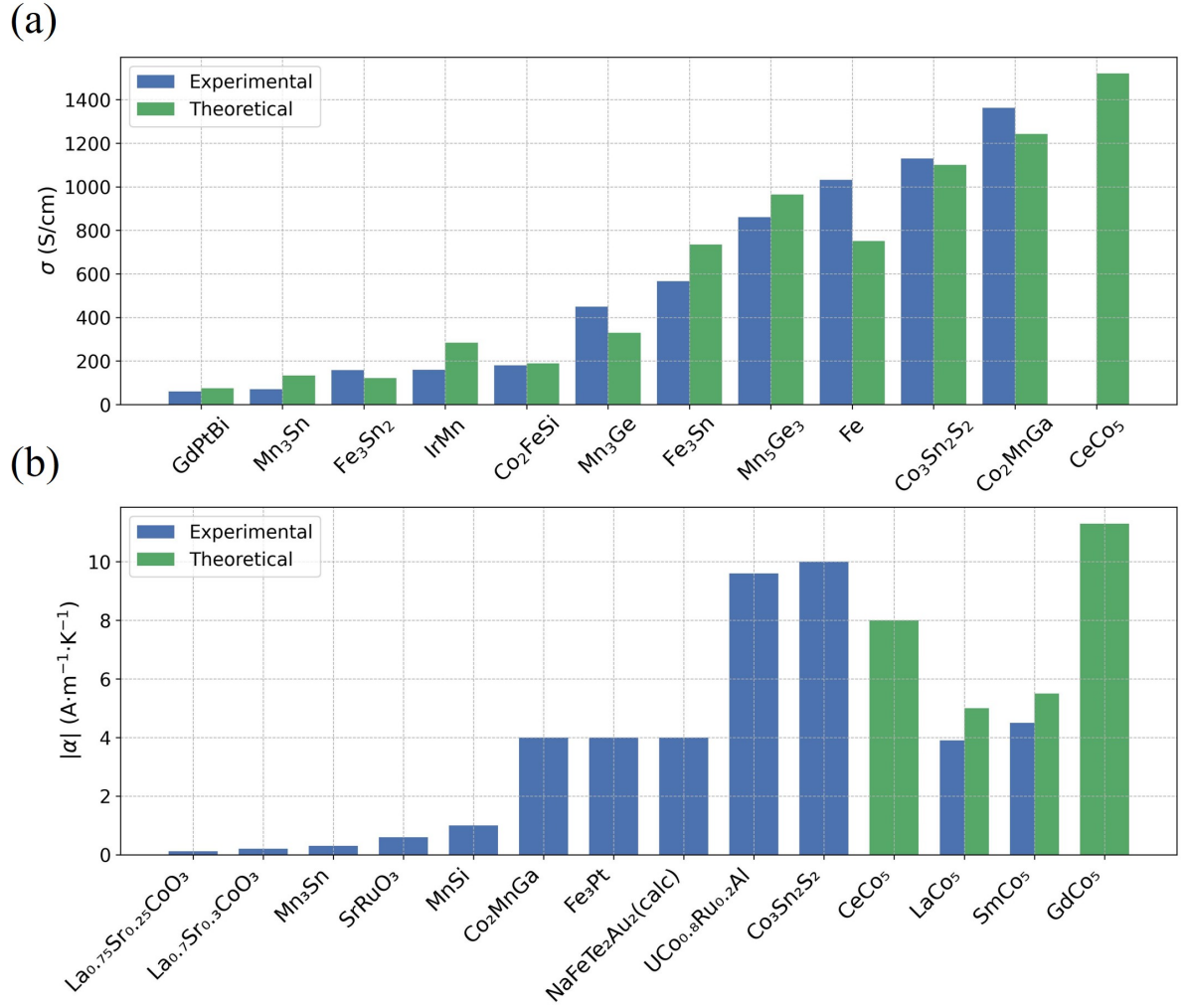


Figure 8: Comparison of AHC and ANC across different materials. Comparison of our results and previously reported data for other materials. The reported data were taken from references [18,33–35,39,62–78] that can also be found in the supplementary materials [48]. Unless otherwise noted, the AHC values shown correspond to the intrinsic Berry-curvature contribution obtained either experimentally or theoretically.